ChemPubSoc Europe

DOI: 10.1002/cctc.201901674

CHEMCATCHEM Full Papers

Check for updates

18673899, 2020, 3, Downloaded from https://chemistry-europe.onlinelibrary.wiley.com/doi/10.1002/cctc.201901674 by Justus-Liebig-Universitat, Wiley Online Library on [01/11/2022]. See the Terms and Conditions (https://onlinelibrary.wiley.com/terms-and-conditions) on Wiley Online Library for rules of use; OA articles are governed by the applicable Creative Commons License

Visualizing Potential-Induced Pitting Corrosion of Ultrathin Single-Crystalline IrO_2(110) Films on RuO_2(110)/Ru(0001) under Electrochemical Water Splitting Conditions

Tim Weber,[a, b] Till Ortmann,[a] Daniel Escalera-López,[c] Marcel J. S. Abb,[a, b] Boris Mogwitz,[a, b] Serhiy Cherevko,[c] Marcus Rohnke,[a, b] and Herbert Over*[a, b]

Sophisticated IrO_2(110)-RuO_2(110)/Ru(0001) model electrodes are employed in the oxygen evolution reaction (OER) under acidic conditions. The potential-induced pitting corrosion of such electrodes is confirmed by a variety of experimental techniques, including scanning electron microscopy (SEM), time-of-flight secondary ion mass spectrometry (ToF-SIMS), and operando scanning flow cell-inductively coupled plasma mass spectrometry (SFC-ICP-MS). The structure of the pits is reminiscent of a cylinder (evidenced by focused ion beam scanning electron microscopy: FIB-SEM), where the inner surface of the pits is covered by hydrous RuO_2 (cyclic voltammetry, ToF-SIMS) that is formed by electrochemical oxidation of the metallic Ru (0001) substrate. The time evolution of the corrosion process at a fixed electrode potential (1.48 V vs. SHE) is followed via cyclic voltammetry and SEM. The passivating IrO_2(110) layer results in an "induction period" for the pit growth that is followed by rapid corrosion of the RuO_2(110)/Ru(0001) substrate. The observed narrow and time-independent size distribution relative to the mean size of the pits is attributed to a sluggish removal of the corrosion products by diffusion across the cracks of the pits covering IrO_2 layer, leading to steady state corrosion during a total polarization time of 20 to 60 minutes.

1. Introduction

In electrocatalysis missing or insufficient stability of the catalyst[1,2] is a major concern that occurs for instance in the anodic half reaction of electrochemical water splitting,[3] where oxygen is evolved (OER: oxygen evolution reaction) as the counter half reaction to the desired hydrogen evolution reaction (HER) at the cathodic side. The OER is a coupled four-electron proton process with sluggish reaction kinetics that requires the use of efficient (active and stable) catalyst materials. Currently, IrO_2 and RuO_2 are the state-of-the-art catalysts for the OER in acidic environments. RuO_2 is the most active electrocatalyst, albeit with insufficient long-term stability, while IrO_2 is somewhat less active,[4] but substantially more stable than RuO_2.[5–7]

Over the past decade, fundamental understanding in electrocatalytic activity has been pushed forward by ab initio methods,[8–10] although the underlying approximations have hardly been validated against benchmark experiments.[11] Ab initio methods for stability issues in electrocatalytic reactions are just emerging.[12–15] Therefore, to deepen our understanding of the molecular processes in electrocatalysis (activity and stability), kinetic and structural studies of well-defined model electrode materials with low structural complexity are required. These experiments can ultimately serve as benchmarks for theoretical ab initio methods, thereby allowing to validate and to advance the theoretical methodology.

Recently, a dedicated model electrode consisting of a single-crystalline IrO_2(110) layer that fully covers a structure-directing template RuO_2(110)/Ru(0001)[16] was developed to study the electrocorrosion under OER conditions.[17] The alterations of the crystalline structure and morphology of the IrO_2(110) film were followed upon anodic polarization, employing a combination of powerful in situ synchrotron radiation based techniques including X-ray reflectivity (XRR) and surface X-ray diffraction (SXRD) and most notably ex situ techniques such as scanning electron microscopy (SEM) and X-ray photoelectron spectroscopy (XPS). In this study the potential-induced pitting corrosion of the ultrathin capping layer IrO_2(110) on RuO_2(110)/Ru(0001) was observed when a pulse-rest potential protocol was applied, where the electrode potential was stepwise increased from 1.30 to 1.94 V vs. the standard hydro-

[a] T. Weber, T. Ortmann, M. J. S. Abb, Dr. B. Mogwitz, Dr. M. Rohnke, Prof. H. Over
Institute of Physical Chemistry
Justus Liebig University
Heinrich-Buff-Ring 17
Giessen 35392 (Germany)
E-mail: Herbert.Over@phys.chemie.uni-giessen.de
[b] T. Weber, M. J. S. Abb, Dr. B. Mogwitz, Dr. M. Rohnke, Prof. H. Over
Center for Materials Research
Justus Liebig University
Heinrich-Buff-Ring 16
Giessen 35392 (Germany)
[c] Dr. D. Escalera-López, Dr. S. Cherevko
Helmholtz Institute Erlangen-Nürnberg for Renewable Energy (IEK-11)
Forschungszentrum Jülich GmbH
Egerlandstr. 3
Erlangen 91058 (Germany)

Supporting information for this article is available on the WWW under https://doi.org/10.1002/cctc.201901674

This publication is part of a Special Collection on "Advanced Microscopy and Spectroscopy for Catalysis". Please check the ChemCatChem homepage for more articles in the collection.

© 2019 The Authors. Published by Wiley-VCH Verlag GmbH & Co. KGaA. This is an open access article under the terms of the Creative Commons Attribution License, which permits use, distribution and reproduction in any medium, provided the original work is properly cited.

gen electrode (SHE) and held for 80 s each potential. In situ XRR and SXRD experiments were performed in between two pulses at a resting potential of 1.30 V vs. SHE.

An alternative approach to examine the anodic corrosion process is to monitor the corrosion products in the electrolyte solution with operando scanning flow cell-inductively coupled plasma mass spectrometry (SFC-ICP-MS), that has shown to be extraordinarily sensitive.[7] For the layered model electrode system IrO_2(110)-RuO_2(110)/Ru(0001), dissolved Ir and Ru species can be monitored and quantified separately.

Both experimental approaches are complementary to some extent, although the viewpoint on the corrosion process is fundamentally different. While the operando SFC-ICP-MS method addresses the corrosion process from the product side, in situ structural methods in combination with ex situ SEM follow the process from the educt side and how the structure (thickness, crystallinity) and morphology of the active part of the electrode is varying in the course of corrosion.

From the previous corrosion study of the IrO_2(110)-RuO_2(110)/Ru(0001) model electrode[17] there have been important scientific questions left that need to be settled: i) What are the structure, morphology and chemical composition of the pits? ii) How does the initial corrosion process on the microscopic scale proceed? iii) How do the pits start to form and expand both laterally and vertically into the substrate with time?

In this study we present ex situ SEM results to follow and to quantify the potential-induced corrosion progress with increasing corrosion time at a fixed electrode potential. This time series can be the starting point to validate a proposed reaction mechanism for the corrosion process. The three-dimensional structure of the pits is reconstructed from focused ion beam scanning electron microscopy (FIB-SEM) and time-of-flight secondary ion mass spectrometry (ToF-SIMS) experiments. Accompanying SFC-ICP-MS experiments allow us to disentangle the contributions of Ir and Ru dissolution/removal in the corrosion process that can be correlated with the induced morphology changes disclosed in the post SEM experiment.

Experimental Section

The IrO_2(110)-RuO_2(110)/Ru(0001) model electrodes were prepared under ultra-high vacuum conditions as described previously.[16] Briefly summarized, the RuO_2(110) layer serving as a template was grown epitaxially on a single-crystalline hat-shaped Ru(0001) disk (4.7 mm diameter, MaTecK, Jülich, Germany).[18,19] Subsequently iridium was deposited on the RuO_2(110)/Ru(0001) template by physical vapor deposition (PVD) utilizing an electron beam evaporator (EMF 3, Omicron). Iridium was oxidized at 700 K during deposition ($p(O_2) = 3\times10^{-7}$ mbar) and additionally postoxidized in 10^{-5} mbar of O_2. The single-crystalline IrO_2(110) films are fully covering the model electrode surface, so that there is no Ru 3d signal visible in the XP spectra (cf. Figure S1 of the Supporting Information). Since the preparation conditions of the samples were identical to those of a previous contribution we assume the thickness of the IrO_2(110) films to be ~10 nm.[17] The model electrodes were studied in two different ways which are explained in the following.

The first sample, denoted here as IrO_2(SFC), was studied with a scanning flow cell-inductively coupled plasma mass spectrometer (SFC-ICP-MS) custom setup following the procedures reported previously.[20] Briefly, a Perkin Elmer NexION 300x ICP-MS was calibrated daily with four standard solutions containing known elemental amounts of Ir and Ru (Merck Certipur) using 20 $\mu g \cdot L^{-1}$ ^{187}Re and ^{103}Rh as internal standards. After calibration, the ICP-MS was connected by means of Tygon tubing (380 µm internal diameter) to the LabVIEW-controlled SFC setup, comprising a Gamry Reference 600 potentiostat (Gamry, USA), a double-junction Ag/AgCl reference electrode compartment (Metrohm, Switzerland; outer compartment filled with 0.1 M HClO4, inner compartment with standard 3 M KCl electrolyte) and a graphite rod counter electrode compartment (6 mm diameter, 99.995 %, Sigma-Aldrich). The V-shaped flow cell employed, CNC machined from a polycarbonate block (CAM 4–02 Impression Gold, vhf camfacture AG, Germany) presented an opening of 0.033 cm^2, effectively defining the working electrode area. The freshly made 0.1 M $HClO_4$ electrolyte (70 %, Suprapur, Merck; pH = 1) was pumped from a reservoir connected to the SFC setup downstream towards the ICP-MS pump at a flow rate of 220 $\mu L \cdot min^{-1}$. All electrolytes used in SFC-ICP-MS measurements were prepared using ultrapure water (MilliQ IQ 7000, Merck).

After the SFC-ICP-MS experiment the electrode surface was characterized by means of scanning electron microscopy (SEM: Zeiss Merlin apparatus). The SE micrographs were obtained with the secondary electron detectors (InLens or SE2), the accelerating voltage was 2 kV while the probe current was 100 pA. After surface characterization the sample was further treated galvanostatically at a fixed current density of 5 $mA \cdot cm^{-2}$ (cutoff value of the potential scan during the SFC-ICP-MS experiment). For this purpose the sample was placed in an electrochemical (EC) glass cell utilizing a hanging-meniscus rotating disk electrode (RDE) setup so that only the IrO_2(110) surface was exposed to the electrolyte solution, a 0.5 M H_2SO_4 solution (pH = 0.4) prepared from H_2SO_4 (Suprapur; Merck, Darmstadt, Germany) and ultrapure water (Milli-Q Direct 8, Merck). An Ag/AgCl electrode (sat. KCl) was used as reference electrode while the counter electrode consisted of a glassy carbon rod. The potential values are given with respect to the standard hydrogen electrode (SHE) throughout the paper. Prior to the electrochemical measurements the electrolyte solution was degassed by flushing with argon while during the measurements the atmosphere above the solution was kept in argon. As galvanostat either a PGSTAT302 N (Autolab-Metrohm) or a SP-150 (BioLogic Science Instruments) was employed. After galvanostatic treatment the electrode surface was again characterized via SEM. This sequence of galvanostatic treatment and surface characterization was repeated several times. In addition, at certain points the electrode surface was studied via time-of-flight secondary ion mass spectrometry (ToF-SIMS) and focused ion beam scanning electron microscopy (FIB-SEM).

For ToF-SIMS analysis a ToF-SIMS 5–100 (IonTOF GmbH, Münster, Germany) was employed. The primary ion gun was operated in burst alignment mode with 25 keV Bi^+ ions as analysis species (I = 0.44 pA @ 55 µs cycle time). The 50×50 μm^2 probing area was scanned with 512×512 pixels. Two depth profiles were carried out with 500 eV Cs^+ ions (I = 41.1 nA), one in interlaced mode with a crater size of 170×170 μm^2 and another one in non-interlaced mode with a crater size of 150×150 μm^2. Data evaluation was conducted with the Surface Lab 7.0 software (IonTOF Company). The obtained mass resolution is $m/\triangle m$ = 180 @ m/z 117.9 (RuO^-). For distinct mass assignment exemplary measurements were conducted in delayed extraction mode. Here the mass resolution is $m/\triangle m$ = 1393 @ m/z 117.9 (RuO^-). FIB-SIMS cuts were prepared with 30 keV Ga^+ ions, I = 5.6 nA. Core milling of the FIB craters was

© 2019 The Authors. Published by Wiley-VCH Verlag GmbH & Co. KGaA

18673899, 2020, 3, Downloaded from https://chemistry-europe.onlinelibrary.wiley.com/doi/10.1002/cctc.201901674 by Justus-Liebig-Universitat, Wiley Online Library on [01/11/2022]. See the Terms and Conditions (https://onlinelibrary.wiley.com/terms-and-conditions) on Wiley Online Library for rules of use; OA articles are governed by the applicable Creative Commons License

carried out with a 300 µm aperture and dwell time of 50 ms with 512×512 pixels and 10 milling scans. For fine milling the 100 µm aperture was used (dwell time 30 ms, 512×512 pixels, 3 milling scans).

For FIB-SEM experiments a DualBeam XEIA3 Triglav microscope (TESCAN) with a Xe-plasma FIB was employed. The milling and polishing was done in one step with Xe^+ ions at an energy of 30 keV (I = 18 nA). SE micrographs of the FIB cut were subsequently recorded within the Zeiss Merlin apparatus.

On the second sample, denoted here as IrO_2(SEM), the progress of the potential-induced pitting corrosion was systematically studied by means of cyclic voltammetry and SEM. The experimental setup for electrochemistry was the same as described above for the galvanostatic treatment. As potentiostat a PGSTAT302 N (Autolab-Metrohm) was employed, equipped with modules enabling electrochemical impedance spectroscopy (EIS) and true analog voltage sweeps. For a systematic investigation of the potential-induced pitting corrosion the model electrode was polarized to 1.48 V vs. SHE (the potential at which the pitting corrosion starts[17]) for a certain time. Subsequently, the sample was characterized via cyclic voltammetry, removed from the EC cell and transferred to the SEM apparatus (Zeiss Merlin) to obtain SE micrographs of the electrode surface. The micrographs were obtained with the secondary electron detectors (InLens or SE2), the acceleration voltage was 2 kV and the probe current was 100 pA. This protocol was repeated several times up to a total polarization time of 82 min. Within the sequence of experiments it was realized that macroscopic oxygen bubbles formed during the polarization. For this reason, during the last four polarization steps the sample was rotated to remove evolving, macroscopic oxygen bubbles.

2. Experimental Results

Recently, the IrO_2(110)-RuO_2(110)/Ru(0001) system was employed as a model electrode to gain insight into corrosion processes under OER conditions. The IrO_2(110) film exhibits a roughness on the mesoscale (yet the terraces are atomically flat) in a regular array reminiscent of "roofs":[16,17] there is a sequence of ascending terraces up to the top of the roof that is followed by a symmetric descending series of terraces. For this reason we have introduced the term "rooflike structure" in our previous study.[17] Due to this rooflike structure of the IrO_2(110) film the corrosion of the model electrode could be studied on different length scales ranging from atomic (in situ SXRD/XRR) to mesoscale (ex situ SEM).[17] Based on these studies it was concluded that the IrO_2(110) film is remarkably stable against anodic corrosion in the OER potential region, while the degradation of the model electrode proceeds via potential-induced pitting corrosion. Ex situ SEM experiments revealed that the corrosion is initiated by Ir dissolution at so-called "surface grain boundaries" where rotational domains of the IrO_2(110) film meet. Once the underlying RuO_2(110)/Ru(0001) is reached, pitting corrosion is accelerated due to the instability of RuO_2 and Ru under these anodic conditions.[17] A schematic representation of resulting pits is shown in Figure 1.

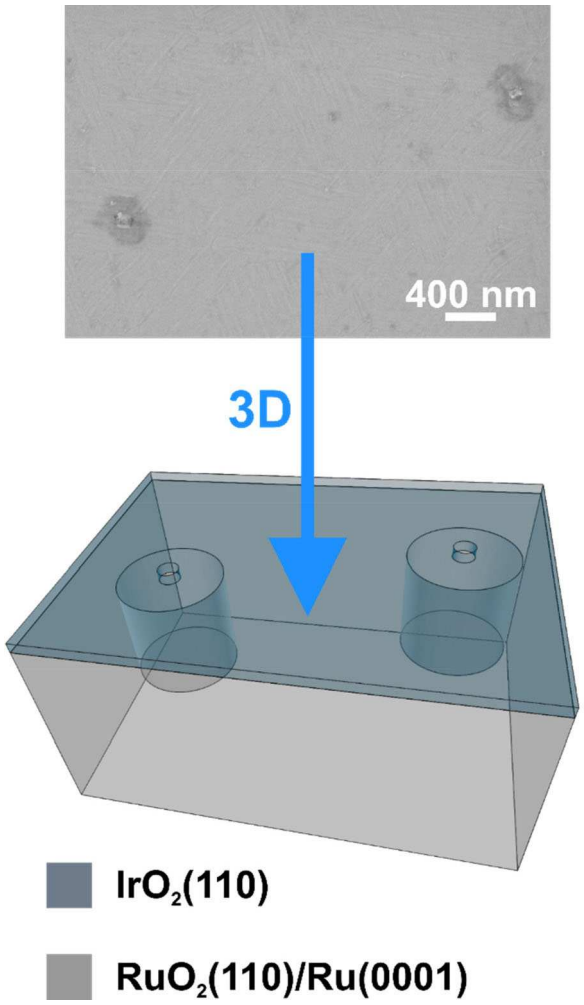

Figure 1. SE micrograph (InLens) of the pitted IrO_2(110)-RuO_2(110)/Ru(0001) model electrode surface (top) and corresponding schematic, three-dimensional representation (bottom).

2.1. IrO_2(SFC)

The SFC-ICP-MS setup allows to follow operando electrochemical dissolution processes. This technique was applied to the IrO_2(110)-RuO_2(110)/Ru(0001) model electrode to gain insight into the corrosion process from analysis of dissolved Ir and Ru species in the electrolyte solution. An overlay of the acquired data is provided in Figure 2a. The dissolution profiles at a magnified scale can be found in Figure S2 of the Supporting Information (SI).

The top and middle panels of Figure 2a display the electrode potential testing protocol selected for SFC-ICP-MS measurements and the corresponding recorded current densities normalized to the geometric surface as a function of time, respectively, while the bottom panel depicts the resulting dissolution rates of Ir (green) and Ru (blue). First, the electrode is held at open-circuit potential (OCP) for 5 min (cf. top of Figure 2a) to approach and contact the SFC with the IrO_2(110)-RuO_2(110)/Ru(0001) model electrode, as seen by the sudden electrode potential drop from ca. 2 V to ca. 0.69 V vs. SHE after

© 2019 The Authors. Published by Wiley-VCH Verlag GmbH & Co. KGaA

18673899, 2020, 3, Downloaded from https://chemistry-europe.onlinelibrary.wiley.com/doi/10.1002/cctc.201901674 by Justus-Liebig-Universitat, Wiley Online Library on [01/11/2022]. See the Terms and Conditions (https://onlinelibrary.wiley.com/terms-and-conditions) on Wiley Online Library for rules of use; OA articles are governed by the applicable Creative Commons License

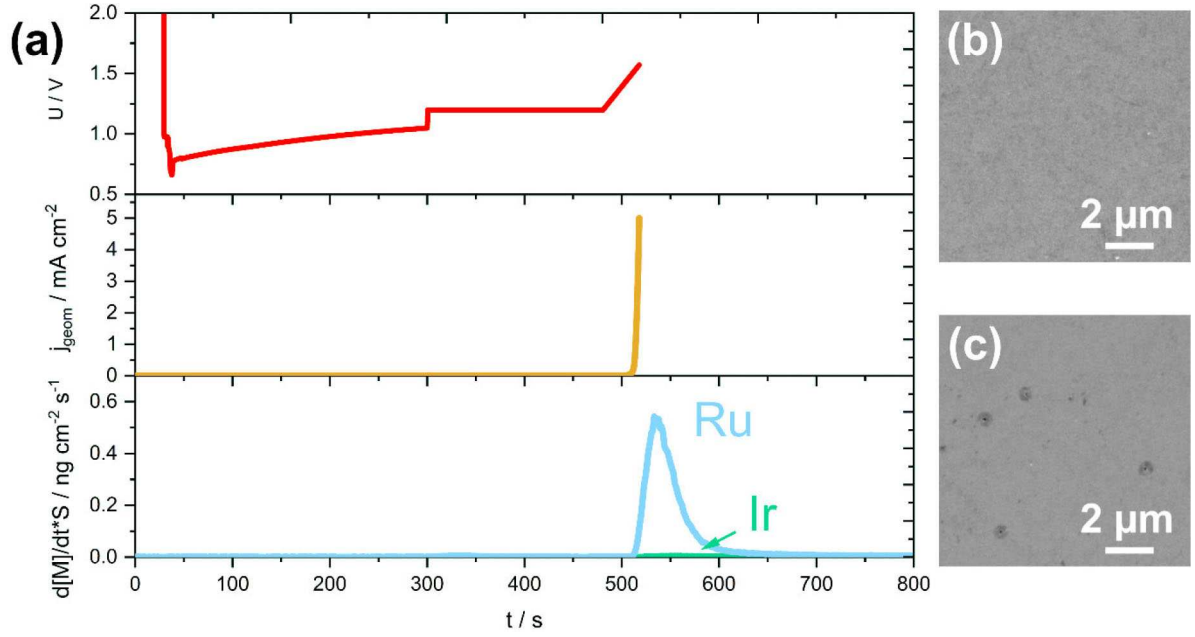

Figure 2. (a) Overlaid SFC-ICP-MS data of the IrO_2(110)-RuO_2(110)/Ru(0001) model electrode. [M] refers here to the monitored metal element dissolution, in this work either Ir or Ru. (b) SE micrograph (InLens) of the freshly prepared electrode surface and (c) SE micrograph (InLens) of the electrode surface after the SFC-ICP-MS experiment.

contact. Since no dissolution peak arising from SFC contact is visible in the ICP-MS data (cf. bottom of Figure 2a), this indicates that the IrO_2(110)-RuO_2(110)/Ru(0001) electrode does not present intrinsically unstable surface defects or native oxides prone to chemical dissolution once in contact with the acidic electrolyte employed.[21] Subsequently the electrode is set to a potential of 1.141 V vs. SHE (1.2 V vs RHE, pre-OER potential) for 3 min (cf. top of Figure 2a). Previous studies have shown that cathodic dissolution is negligible for thermally prepared IrO_2,[7] whereas for anodically formed IrO_2 its experimental onset potential is 1.041 V vs. SHE.[22] Induced by this potential variation there are dissolution peaks (cf. bottom of Figure 2a) arising for both Ir (0.065 ± 0.004 ng·cm^{-2}) and Ru (0.4 ± 0.2 ng·cm^{-2}). These peaks decline with time to the baseline within the potentiostatic hold, indicating that steady-state dissolution is not present. The transient dissolution may be due to restructuring of the oxides[23] and/or dissolution of iridium exposed in surface grain boundaries.[17] Next, the electrode potential is scanned positively at a 10 mV·s^{-1} scan rate until a cutoff current density value of 5 mA·cm^{-2} is reached (cf. middle of Figure 2a) after which the potential is set back to OCP. During this potential scan dissolution is observed for both Ir and Ru (cf. bottom of Figure 2a), with dissolution onset potentials estimated at 1.50 ± 0.02 V and 1.47 ± 0.1 V, respectively. It is noteworthy that the total dissolution for Ir (0.24 ± 0.04 ng·cm^{-2}) is almost two orders of magnitude lower than that for Ru (20.4 ± 0.8 ng·cm^{-2}).

Given the well-defined, layered and highly-crystalline nature of the IrO_2(110)-RuO_2(110)/Ru(0001) electrode, we can also normalize the dissolution to the working electrode area, with values of 0.075% and 12.1% for Ir and Ru, respectively (a comment on the calculation of the monolayer normalized dissolution can be found in the SI). This result is consistent with the process of potential-induced pitting corrosion, where the total area of cracks in the IrO_2(110) film is small, while the under-corroded region in the Ru(0001) substrate is large and deep. This conclusion is corroborated by means of post SEM analysis of the model electrode surface that reveals small pits (cf. Figure 2c and Figure S3).

After the SCF-ICP-MS experiments the sample was further treated galvanostatically for 4.5 and 17.5 min in total at 5 mA·cm^{-2} and studied by means of ToF-SIMS and FIB-SEM to analyze the shape and the chemical composition of the pits. With a focused ion beam the electrode surface was cut perpendicular to the surface (either within the ToF-SIMS or the FIB-SEM apparatus) to be able to study the depth of the pit. SE micrographs were then acquired and are shown in Figure 3.

Figure 3a shows a SE micrograph of the electrode surface prior to the ion beam cutting. Clearly visible is the rooflike structure of the IrO_2(110) film both at the fully intact surface and the locally undercut region. This is consistent with the previous finding that the rooflike structure on intact domains was not altered due to anodic polarization in the OER potential region.[17] Also clearly visible is a pit in form of the typical ring-shaped contrast around the fractured IrO_2(110) film which is assumed to be due to erosion of the underlying Ru substrate. However, in the previous publication[17] this undercut region was not explored in detail. With FIB cuts perpendicular to the electrode surface it is possible to open the pits and image them with SEM from the side (cf. Figure 3b, c). The dashed white lines indicate the edges of the FIB cuts, while the dotted red line illustrates the shape of the pit. The covering IrO_2(110) film is

© 2019 The Authors. Published by Wiley-VCH Verlag GmbH & Co. KGaA

18673899, 2020, 3, Downloaded from https://chemistry-europe.onlinelibrary.wiley.com/doi/10.1002/cctc.201901674 by Justus-Liebig-Universitat, Wiley Online Library on [01/11/2022]. See the Terms and Conditions (https://onlinelibrary.wiley.com/terms-and-conditions) on Wiley Online Library for rules of use; OA articles are governed by the applicable Creative Commons License

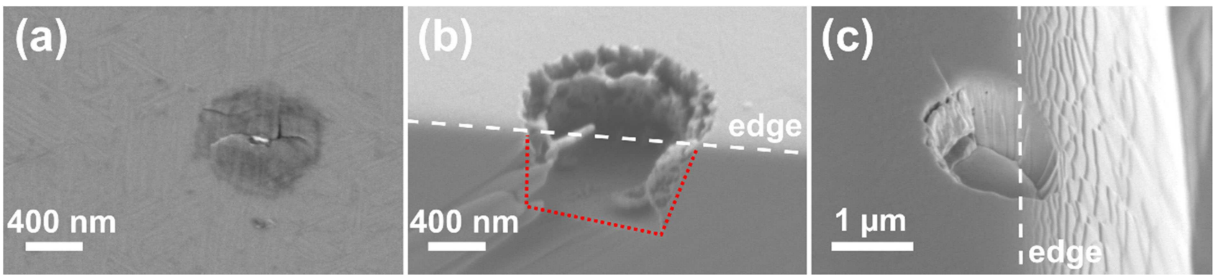

Figure 3. (a) SE micrograph (InLens) of a pit at the electrode surface. (b) SE micrograph (SE2, stage tilted by 40°) of a pit truncated by a FIB cut (Ga^+ ions) done within the ToF-SIMS apparatus. The FIB cut was applied after 4.5 min at 5 mA·cm^{-2}. (c) SE micrograph (InLens, stage tilted by 30°) of a pit truncated by a FIB cut (Xe^+ ions) done within the FIB-SEM apparatus. The FIB cut was applied after 17.5 min at 5 mA·cm^{-2}. The dashed white lines indicate the edges of the FIB cuts while the dotted red line illustrates the shape of the pit.

removed by the focused ion beam, but the local erosion of the Ru(0001) substrate becomes now clearly visible, whose three-dimensional shape is reminiscent of a cylinder. From Figure 3b, c it seems that the pit walls perpendicular to the electrode surface are porous, while the base area is plain. The observed porosity is reconciled with electrochemically formed hydrous RuO_2 at the pit walls. From the profile of the pit in the SEM image (cf. Figure 3b) the radius fairly coincides with its depth. This might indicate that the corrosion rates of the Ru(0001) facet parallel and the Ru(10 $\bar{1}$ 0) facet normal to the IrO_2(110) film are at least comparable.

To gain further information on the chemical composition within the pits, ToF-SIMS was utilized. In principle, we are able to visualize the chemical composition of the layered structure of the IrO_2(110)-RuO_2(110)/Ru(0001) model electrode (cf. Figure S4). However, in the following we rather focus on the chemical composition of the pits than on the layered structure of the model electrode.

In Figure 4 the IrO_2^- (green) and RuO^- (red) mass signals of ToF-SIMS depth profiles are overlaid; additional mass signals are provided in Figures S5 and S6. The profile in Figure 4a is 2.9 µm deep, depicting the pits completely in terms of their depth. The profile was recorded in interlaced mode, therefore the IrO_2(110) layer does not fully cover the surface anymore. In contrast, the profile (1 µm deep) shown in Figure 4b was recorded in non-interlaced mode so that the IrO_2(110) layer is visible within the total scanned area. The difference between interlaced and non-interlaced mode is the usage of the sputtergun. In interlaced mode the sputtergun operates during the deadtime, that is when the ions are passing the time-of-flight tube. After scanning half of the sample area the topmost IrO_2 layer is already removed by sputtering. In non-interlaced mode a complete analysis scan of one layer is carried out before the sputtergun erodes the sample area further. The IrO_2^- mass signal with its high intensity at the top region clearly displays the IrO_2(110) film at the electrode surface. In contrast, the RuO^- mass signal illustrates channel-like structures that are assigned to be the pits. The detection of RuO^- ions indicates the presence of electrochemically formed hydrous RuO_2 at the inner surface of the pits. Additionally, the O^- mass signal (cf. Figures S5 and S6) can be utilized to image both the oxide film at the surface and the pits formed due to anodic corrosion. Even the C^- mass signal can be employed to image the pits, due likely to CO_2 that is dissolved in the hydrous RuO_2 layer[24,25] at the inner surface of the pits.

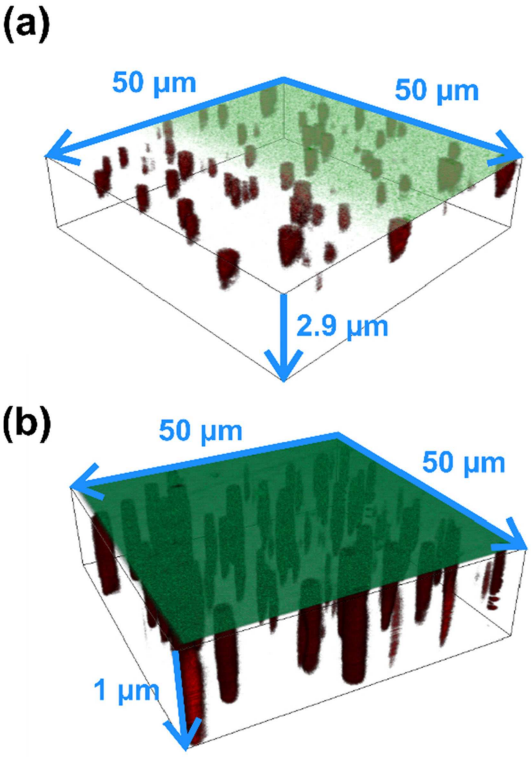

Figure 4. 3D maps recorded within two depth profiles utilizing ToF-SIMS of the model electrode after galvanostatic treatment at 5 mA·cm^{-2} for 17.5 min in total: a) interlaced mode and b) non-interlaced mode. The maps show the overlaid mass signals of IrO_2^- (green) and RuO^- (red). The signal intensity increases from black (low intensity) to the respective color (high intensity).

The pits are not visualized as structures with zero intensity but "filled". This can be explained by the primary ion beam impinging on the sample surface at an angle of 45°. For this reason in the pit region the beam ends up at the inner wall of a pit. Due to their trajectory the emitted secondary ions are detected in the center of the pit. A graphical representation of this effect can be found in the SI (cf. Figure S7).

© 2019 The Authors. Published by Wiley-VCH Verlag GmbH & Co. KGaA

18673899, 2020, 3, Downloaded from https://chemistry-europe.onlinelibrary.wiley.com/doi/10.1002/cctc.201901674 by Justus-Liebig-Universitat, Wiley Online Library on [01/11/2022]. See the Terms and Conditions (https://onlinelibrary.wiley.com/terms-and-conditions) on Wiley Online Library for rules of use; OA articles are governed by the applicable Creative Commons License

2.2. IrO_2(SEM)

The IrO_2(110)-RuO_2(110)/Ru(0001) model electrode was polarized at 1.48 V vs. SHE and a time series of SE micrographs of the electrode surface was acquired. Already from the current increase in the single chronoamperometry experiments (cf. Figure S8) we can conclude that the electrode surface corrodes. The increase in current density with polarization time is due partly to the high OER activity of hydrous RuO_2 that is formed at the pit walls during corrosion. After each polarization step (for a specific time period) the electrode surface was characterized by means of cyclic voltammetry and ex situ SEM. Figures 5 and 6 compile SE micrographs for various total polarization times.

As visualized in Figure 5 the first pits appear after 630 s of polarization with a diameter of a few hundred nanometers, so that it seems that there is a kind of "induction period" of at least 310 s which is needed for the pits to form. Between 310 s and 630 s no SE micrographs are available since at the beginning of the time series the duration of the single polarization steps was doubled each step (starting from 10 s) until the first pits appeared. From Figure 5 we recognize that the lateral shape of the pits is approximately a disk, its diameter increases with total polarization time. After a total polarization time of 82 min the pit's diameter reaches about 3–4 µm. The IrO_2(110) film covering the pits exhibits cracks which might be caused by mechanical stress due to oxygen bubbles forming in the pits or by the relief of internal strain in the IrO_2(110) layer. In addition, the number of pits is increasing with total polarization time as summarized in Figure 6. However, with increasing their diameter the pits are merging at a certain point (cf. Figure 6, after 72 min and 82 min).

The SE micrographs are quantitatively evaluated utilizing the software package ImageJ[26] (v. 1.52a). After each polarization step ten SE micrographs were recorded at a magnification of 3,000× for evaluation. When the area of the pits had increased so that they became visible at lower magnifications, ten additional SE micrographs each were recorded at magnifications of 1,000× and 2,000× additionally. The determination of pit area and the number of pits is based on the intensity contrast due to the pits and the resulting differences in their grayscale. ImageJ allows to select a particular grayscale range of a grayscale picture and to convert it to a black-and-white picture. After that the pits are enumerated applying the software's feature "*analyze particles*" while the pixel size is calibrated to the scale bar of the micrographs. In order to avoid erroneous counts, structures on the surface appearing black or in a similar grayscale range as the pits (but not being pits) are

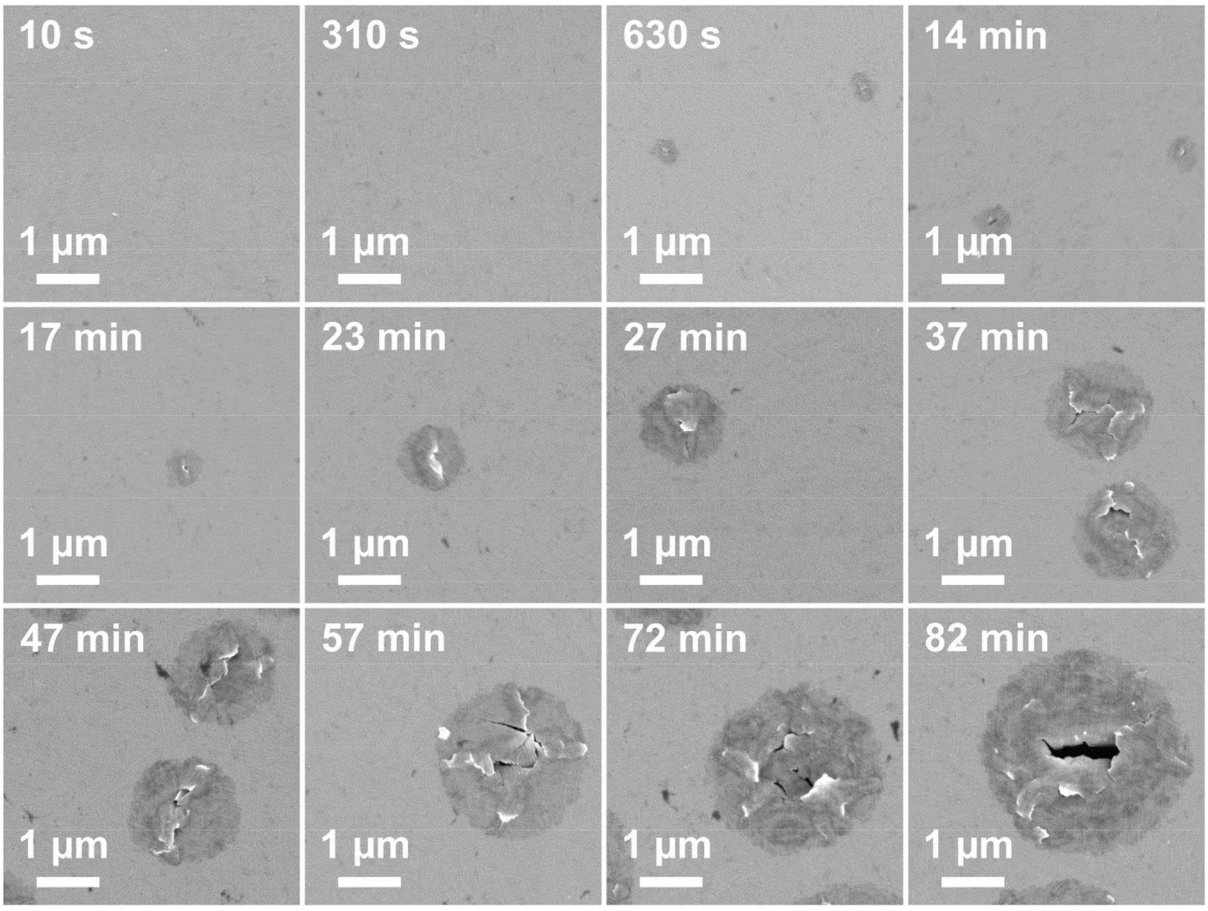

Figure 5. SE micrographs (all InLens) of the model electrode surface in dependence of the total polarization time at 1.48 V vs. SHE. The first small pits appear after 630 s.

© 2019 The Authors. Published by Wiley-VCH Verlag GmbH & Co. KGaA

18673899, 2020, 3, Downloaded from https://chemistry-europe.onlinelibrary.wiley.com/doi/10.1002/cctc.201901674 by Justus-Liebig-Universitat, Wiley Online Library on [01/11/2022]. See the Terms and Conditions (https://onlinelibrary.wiley.com/terms-and-conditions) on Wiley Online Library for rules of use; OA articles are governed by the applicable Creative Commons License

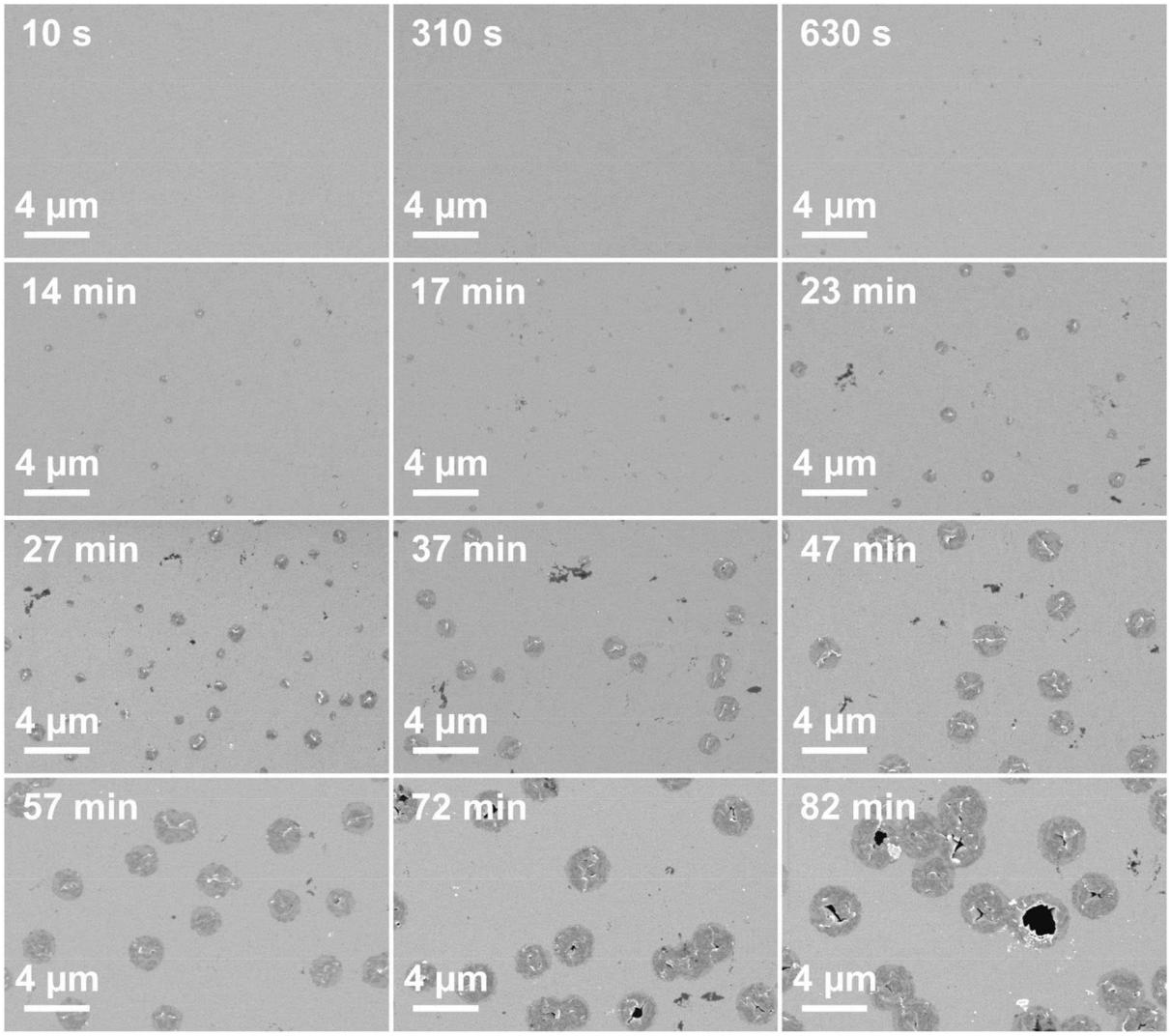

Figure 6. SE micrographs (all InLens) of the model electrode surface in dependence of the total polarization time at 1.48 V vs. SHE.

cut out prior to the evaluation and a threshold value for the minimal pit area is set. In addition, fragmentarily depicted pits at the edges of the micrographs are excluded from analysis.

Moreover, the voltammetric charge is derived from the cyclic voltammograms (CVs). Here CVs with a potential region from 0.5–1.3 V vs. SHE are used so that only the capacitive current with no OER contribution is evaluated. Figure 7 provides a survey of the derived data, (a)–(c) are based on the evaluation of the SE micrographs, whereas (d) gives the voltammetric charge derived from the CVs.

The mean pit area and the total pit area relative to the whole electrode surface area (cf. Figure 7a, c) are increasing steadily with polarization time after a kind of "induction period". The pit density, that is the number of pits per surface area, shows a different time evolution: after the "induction period" the pit density increases, then reaches a plateau and declines afterwards (cf. Figure 7b). From these data one can derive a "mechanism" for the potential-induced pitting corrosion: in the beginning (i) when the electrode surface starts to form pits the number of pits rises abruptly. With total polarization time both the number of pits and the mean pit area increase first (cf. Figure 7a, b and Figures 5, 6), while between 25 min and 50 min (ii) the pit density remains roughly constant albeit the mean pit area is still growing. Therefore, the existing pits are growing in diameter while only few pits are newly formed. With ongoing polarization the pit density decreases (iii) which can be explained by merging pits (cf. Figure 5). This causes ImageJ to count pits connected by at least one pixel as a single pit so that the number of pits apparently declines. However, within the time period (ii) (cf. Figure 7b) there is no significant merging of pits observed.

With SEM we monitor the changes in surface morphology of the model electrode, while electrochemical alterations are monitored with cyclic voltammetry. Figure 7d shows the voltammetric charge as a function of the total polarization time. The series of cyclic voltammograms can be found in Figure S9. The mean pit area, the total pit area and the voltammetric charge are steadily increasing with total polarization time.

© 2019 The Authors. Published by Wiley-VCH Verlag GmbH & Co. KGaA

18673899, 2020, 3, Downloaded from https://chemistry-europe.onlinelibrary.wiley.com/doi/10.1002/cctc.201901674 by Justus-Liebig-Universitat, Wiley Online Library on [01/11/2022]. See the Terms and Conditions (https://onlinelibrary.wiley.com/terms-and-conditions) on Wiley Online Library for rules of use; OA articles are governed by the applicable Creative Commons License

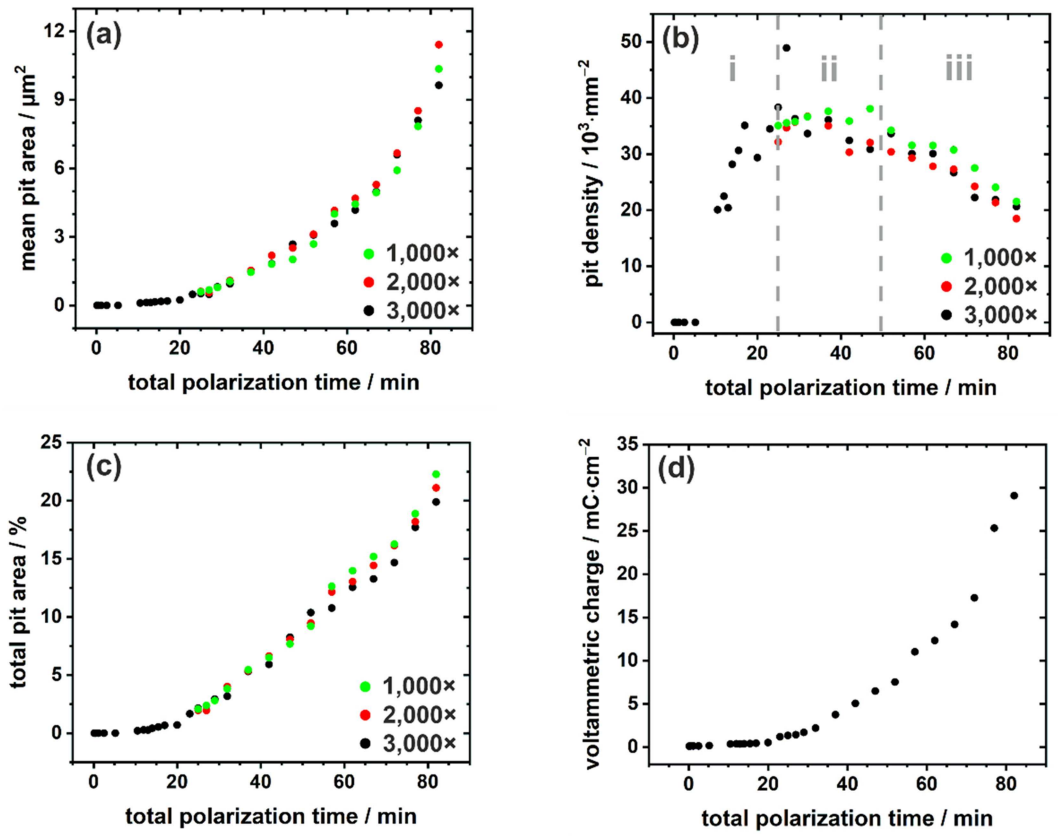

Figure 7. (a) Mean area of the pits, (b) number of pits per surface area, (c) relative pit area with respect to the total surface area and (d) voltammetric charge as derived from the CVs as a function of the total polarization time at 1.48 V vs. SHE. The legend in (a)–(c) gives the different magnifications of the respective SE micrographs used for the evaluation.

When comparing the mean pit area and the voltammetric charge as a function of polarization time in Figure 7 a, d one can recognize a very similar behavior. This is reconciled with a linear behavior of the voltammetric charge, derived from the CVs, as a function of the mean pit area (cf. Figure 8).

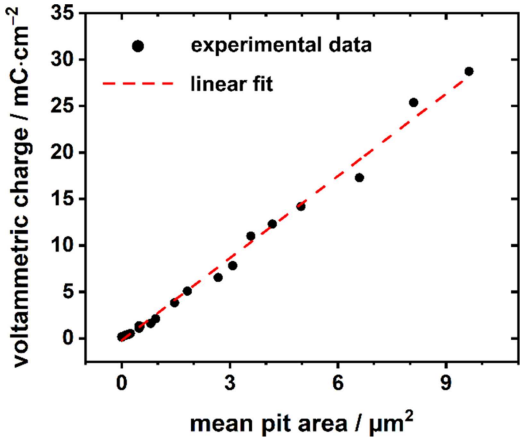

Figure 8. Voltammetric charge as derived from the cyclic voltammograms as a function of the mean pit area (as derived from the SEM series at a magnification of 3,000×). A linear correlation can be established.

From visual inspection of Figure 6 the size distribution of the pits is surprisingly narrow throughout the time series. This impression can further be analyzed via a time series of histograms based on the SEM time series, similar to those shown in Figure 6. Each histogram is given in relative units, i. e., size of the pits relative to the averaged size, and a description of how they are derived from the SE micrographs can be found in the SI (cf. Figure S10). A total polarization time higher than 52 min was not subject to analysis since the pits start merging (cf. Figure 7 b (iii)). The histograms are fitted to normal distributions (Gaussian), thereby providing the relative standard deviation (cf. Figure 9) as a measure for the narrowness of the pit size distribution.

These standard deviations of the pit size distributions as a function of the total polarization time, depicted in Figure 9, are roughly constant indicating that the pit size distribution does not change very much with the total polarization time.

3. Discussion

The present contribution provides an in-depth study of the recently recognized potential-induced pitting corrosion process[17] of ultrathin single-crystalline IrO_2(110) films sup-

© 2019 The Authors. Published by Wiley-VCH Verlag GmbH & Co. KGaA

18673899, 2020, 3, Downloaded from https://chemistry-europe.onlinelibrary.wiley.com/doi/10.1002/cctc.201901674 by Justus-Liebig-Universitat, Wiley Online Library on [01/11/2022]. See the Terms and Conditions (https://onlinelibrary.wiley.com/terms-and-conditions) on Wiley Online Library for rules of use; OA articles are governed by the applicable Creative Commons License

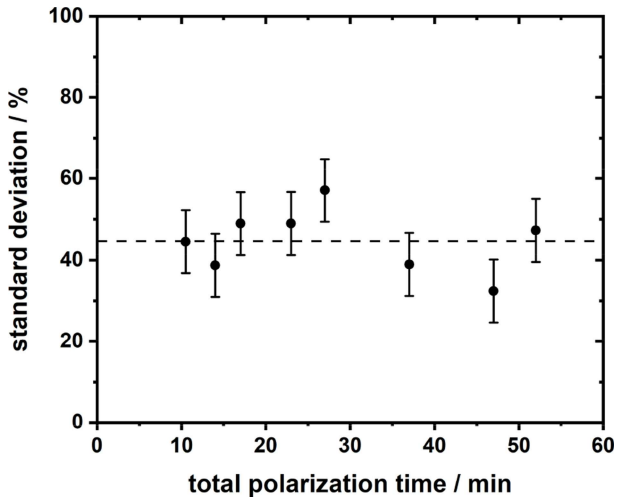

Figure 9. Relative standard deviation of the normal distribution of the relative pit size as a function of the total polarization time. The dashed line indicates the mean value.

ported on a RuO_2(110)/Ru(0001) template, serving as model electrode. In situ synchrotron radiation based techniques (SXRD, XRR) revealed that the IrO_2(110) film was not altered upon anodic polarization up to 1.94 V vs. SHE in terms of thickness, periodicity and domain size. The integral intensity derived from the in situ SXRD data decreased by around 85% though, while ex situ XPS indicated that only around 50% of the initial Ir amount on the electrode surface was lost.[17] This apparent contradiction was unraveled utilizing ex situ SEM which revealed potential-induced pitting corrosion, initiated at so-called surface grain boundaries, to be operative. Therefore, it was concluded that the IrO_2(110) film was disordered rather than dissolved during the in situ experiments.[17] However, the process of potential-induced pitting corrosion of IrO_2(110)-RuO_2(110)/Ru(0001) itself has not been studied in detail yet. The present contribution aims at the elucidation of the corrosion process (cyclic voltammetry, SEM, SFC-ICP-MS) and of the structure and chemical composition of the pits (FIB-SEM, ToF-SIMS). In order to gain insights, we first employ operando SCF-ICP-MS measurements to quantify the amount of Ir and Ru dissolved due to anodic polarization. Second, the three-dimensional morphology of the pits is revealed by FIB-SEM and ToF-SIMS, with ToF-SIMS providing information on the chemical composition within the pits. Third, the temporal evolution of the forming pits is followed by means of cyclic voltammetry and SEM.

The SFC-ICP-MS experiment reveals two dissolution signals of Ir and Ru (cf. Figure 2a). The first signal, which declines to the baseline after a certain time, is due likely to transient dissolution[23] when the electrode potential is held at 1.141 V vs. SHE. This transient dissolution might be correlated with surface grain boundaries with highly under-coordinated Ir atoms that are prone to dissolve. Here the first pits form first, so that a Ru dissolution signal emerges as well. When ramping the electrode potential up to 1.508 ± 0.005 V vs. SHE (at 5 $mA \cdot cm^{-2}$) a second dissolution signal is visible with RuO_2(110)/Ru(0001) exhibiting a total dissolution around two orders of magnitude higher than that of the IrO_2(110) layer (20.4 ± 0.8 $ng \cdot cm^{-2}$ vs. 0.24 ± 0.04 $ng \cdot cm^{-2}$). This trend is in good agreement with analogous experiments previously performed on thermally-oxidized sputtered Ir and Ru thin films, where RuO_2 and IrO_2 total dissolution was 1.9 ± 0.3 $ng \cdot cm^{-2}$ and 0.07 ± 0.01 $ng \cdot cm^{-2}$, respectively.[7] The total dissolution values observed for the IrO_2(110) and the RuO_2(110)/Ru(0001) are, however, one order of magnitude higher than the aforementioned but still significantly lower than those found at an identical voltage ramp protocol for metallic Ru (253 ± 11 $ng \cdot cm^{-2}$) and Ir (8.4 ± 0.3 $ng \cdot cm^{-2}$),[7] as well as electrochemically-grown hydrous Ir oxide films, which range from 8.6 to 25.1 $ng \cdot cm^{-2}$ depending on the number of growth cycles applied to a pristine Ir electrode.[27] Therefore, we can conclude that the discrepancies regarding total Ir and Ru dissolution with respect to those found for rutile RuO_2 and IrO_2 surfaces arise from the potential-induced pitting corrosion mechanism. Besides Ir dissolution from IrO_2(110) surface grain boundaries mechanical instability of the IrO_2(110) layer above the pits may explain the higher total Ir dissolution for IrO_2(110)-RuO_2(110)/Ru(0001), where the experimental Ir dissolution onset (1.50 ± 0.02 V) is in good agreement with the potential under which pitting corrosion was observed (1.48 V vs. SHE).[17] The pitting corrosion process then propagates through the RuO_2(110) layer down to the underlying Ru(0001) substrate, yielding a total dissolution higher than that expected for rutile RuO_2 given the higher instability of the metallic Ru surface, which is more prone to electrodissolution under OER potentials.[7]

After the SFC-ICP-MS experiment the IrO_2(SFC) sample was further treated galvanostatically at a fixed current density of 5 $mA \cdot cm^{-2}$ for certain time steps and the pits were characterized ex situ via FIB-SEM and ToF-SIMS. With FIB-SEM we were able to demonstrate that the Ru substrate is indeed eroded locally, virtually forming cylindrical pits with the depth of the pits roughly equal to its radius *r*. The inner surface of the pits is covered by hydrous RuO_2 as evidenced by 3D mapping via ToF-SIMS (cf. Figure 4), the appearance of the pits in SEM (cf. Figure 3b), and by the increase in voltammetric charge with total polarization time (cf. Figure 7d). Also the ICP-MS data indicate the presence of hydrous RuO_2 since the total Ru dissolution (20.4 ± 0.8 $ng \cdot cm^{-2}$) is significantly higher than what one would expect for rutile RuO_2 (1.9 ± 0.3 $ng \cdot cm^{-2}$). According to the Pourbaix diagram of Ru[28] the metal undergoes electrochemical oxidation to hydrous RuO_2 via a $Ru(OH)_3$ species and at even higher potentials dissolves via formation of soluble Ru (VI) and Ru(VIII) species like RuO_4^{2-} and RuO_4, respectively.[28,29] The thermodynamic stability is reconciled with the time evolution of the pit morphology. As soon as the passivating IrO_2(110) layer breaks down, the Ru metal substrate starts to be electrochemically corroded forming first hydrous RuO_2 that is further oxidized to form soluble Ru species in high oxidation state. In this way the pits form. The lateral and vertical growth of pits proceeds via corrosion of the inner surface of the pits, forming a covering hydrous RuO_2 layer from where soluble Ru species are dissolved.

© 2019 The Authors. Published by Wiley-VCH Verlag GmbH & Co. KGaA

18673899, 2020, 3, Downloaded from https://chemistry-europe.onlinelibrary.wiley.com/doi/10.1002/cctc.201901674 by Justus-Liebig-Universitat, Wiley Online Library on [01/11/2022]. See the Terms and Conditions (https://onlinelibrary.wiley.com/terms-and-conditions) on Wiley Online Library for rules of use; OA articles are governed by the applicable Creative Commons License

From the cylindrical form of the pits we can deduce that the corrosion process perpendicular to the surface normal in ($10\bar{1}0$) and symmetry-equivalent directions is almost independent of the lateral orientation. Would corrosion along the ($10\bar{1}0$) and symmetry-equivalent directions be much slower than other in-plane directions, a hexagonal instead of a disk shape appearance of the pit base would be expected. Quite in contrast, the corrosion process along the surface normal in (0001) direction leads to quite flat base area, indicating that a partially corroded (0001) plane is unstable and rapidly corroded.

From Figure 8 it is clear that the voltammetric charge is proportional to the mean pit area and therefore proportional to r^2, with r being the radius of a pit. The increase in capacitive current and hence the voltammetric charge is indicative of hydrous RuO_2, a well-known supercapacitor material,[30] that is electrochemically formed at the pit walls[17,24] as evidenced by the FIB-SEM data in Figure 3 and the 3D maps obtained from ToF-SIMS in Figure 4. If the shape of a pit is assumed to be cylindrical with the height h of the cylinder being at least proportional to the radius r of the pits (FIB-SEM, cf. Figure 3 b), then the inner surface area of the pits and hence the voltammetric charge is proportional to r^2 as observed in Figure 8.

As summarized in Figure 9, the standard deviation of the relative size distribution of the pits does not vary with polarization time. Since for a "simple" growth mechanism one would expect a broadening of the pit size distribution with growth time (= total polarization time), we infer that the growth "mechanism" of the pits is quite complex. This finding in conjunction with an apparent "induction period" is indicative of at least three processes which take place on very different time scales. During the "induction period" iridium from the IrO_2(110) film might be dissolved at surface grain boundaries, therefore locally thinning the "passivating" oxide layer. This process is presumably slow, since the corrosion rate derived from the SFC-ICP-MS experiment is quite low for the IrO_2(110) film (cf. Figures 2 and S2). Once the significantly less stable RuO_2(110)/Ru(0001) substrate is exposed to the electrolyte solution, the corrosion process is strongly accelerated: the dissolution of Ru proceeds about two orders of magnitude faster than that of Ir (cf. Figures 2 and S2). However, to achieve the observed narrow and constant relative size distribution of pits, the initially fast undercorrosion process must slow down for larger pits. The reason for this deceleration of the corrosion process of Ru may be attributed to a sluggish removal of the corrosion products through the narrow cracks in the IrO_2 layer, namely soluble Ru species with high oxidation states like RuO_4^{2-} and RuO_4.[28,29] As a consequence, the concentration of Ru-based ions is high in the pits, shifting the reversible half-cell potential(s) U_{rev} of the respective Ru redox transition(s) positively. For this reason, the overpotential(s) η, defined as $\eta = U - U_{rev}$ with U being the applied electrode potential, decrease(s) and the resulting corrosion current (density) decreases exponentially, according to Butler-Volmer equation,[11,31] thus narrowing the size distribution.

For large polarization times the corrosion process should reach steady state conditions. The reasons behind this simple model are (i) that the driving force according to Nernst equation diminishes with increasing concentration of dissolved Ru species (as discussed above) and (ii) that the crack area where the dissolved Ru species can escape from the pit is small compared to the wall area of the pit, where metallic Ru is electrochemically oxidized and dissolved and the processes to reach steady state are fast enough. This means that diffusion of the dissolved Ru species in the pits needs to be fast and the transport outside the pits should be even faster to maintain a constant concentration profile across the crack.

A rough estimation based on a typical diffusion coefficient in aqueous solutions of $10^{-5}\ cm^2 \cdot s^{-1}$ leads to a diffusion length of some 100 μm in 100 s, the time resolution of our corrosion experiment. Since the pit dimensions of the undercutting region is in the order of less than 10 μm even after a polarization time of 1 h, steady state can quickly be accomplished by diffusion.

Assuming that the pits are cylindrical with radius r and depth h the molar amount dn of dissolved Ru species per time dt is given by Equation (1)

$$\frac{dn}{dt} = c \cdot 4 \cdot \pi \cdot r(t) \cdot h(t) \cdot \frac{dr}{dt} = j_{dif} \cdot A_{crack} = \text{const.} \quad (1)$$

with c being a constant, describing the molar concentration of Ru in the sample. In steady state the produced amount needs to be identical to that which diffuses through the crack with the area A_{crack} and diffusion flux j_{dif}, given by Fick's second law. This corresponds to a mass balance.

From experiments we know that the depth of the pits h is proportional to the radius of the pits r. Therefore, we can easily solve the differential Equation (1) and obtain Equation (2)

$$r(t)^3 - r(t_0)^3 = c' \cdot (t - t_0) \quad (2)$$

with c′ being a constant. This relation can be reconciled with the experimental values: in the polarization time window between 25 min and 65 min the experimental data from Figure 7 a can be linearly approximated by $r(t)$ as a function of $t^{1/3}$ (cf. Figure 10).

The range where Equation (2) is applicable is roughly the time range where the number of pits is constant. From experiment we obtain $r(t_0) = 0.25$ μm and $t_0 = 25$ min.

4. Conclusions

Recently, the degradation of IrO_2(110)-RuO_2(110)/Ru(0001) model electrodes under oxygen evolution conditions in an acidic environment was shown to proceed via potential-induced pitting corrosion.[17] The present contribution is dedicated to answer important remaining scientific questions regarding structure/morphology and chemical composition of the pits and the time evolution of the corrosion process on the microscopic scale. First, FIB-SEM and ToF-SIMS evidence the

© 2019 The Authors. Published by Wiley-VCH Verlag GmbH & Co. KGaA

18673899, 2020, 3, Downloaded from https://chemistry-europe.onlinelibrary.wiley.com/doi/10.1002/cctc.201901674 by Justus-Liebig-Universitat, Wiley Online Library on [01/11/2022]. See the Terms and Conditions (https://onlinelibrary.wiley.com/terms-and-conditions) on Wiley Online Library for rules of use; OA articles are governed by the applicable Creative Commons License

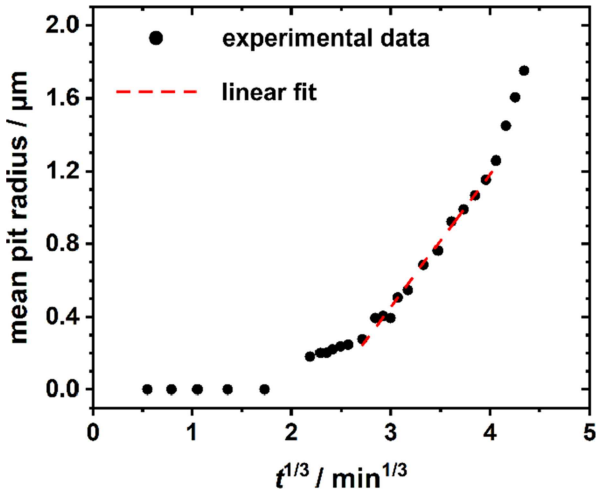

Figure 10. The mean pit radius r as a function of $t^{1/3}$, with t being the total polarization time.

existence of cylinder-shaped pits at the model electrode during the initial stage of potential-induced pitting corrosion. Electrocorrosion of the unstable Ru(0001) substrate is in-plane nearly independent of the direction. Operando analysis of the corrosion products by means of SFC-ICP-MS reveals dissolution of Ir and Ru, therefore the initially fully covering IrO_2(110) film has to be (locally) dissolved or mechanically disrupted so that the electrolyte solution can reach the unstable RuO_2(110)/Ru (0001) substrate. Since post SEM analysis reveals small pits in the model electrode surface we infer that the two orders of magnitude higher Ru than Ir dissolution signal supports pitting corrosion to be operative from the "electrolyte-point of view". Utilizing ToF-SIMS the presence of hydrous RuO_2 within the pits, as already suggested by XPS data,[17] is evidenced. The increase in voltammetric charge as derived from the cyclic voltammograms is attributed to the formation of hydrous RuO_2, a well-known supercapacitor material.[30] From the linear correlation of the voltammetric charge with the mean pit area, we conclude that hydrous RuO_2 grows only at the inner surface of the pits.

Changes in surface morphology and electrochemical behavior at 1.48 V vs. SHE due to potential-induced pitting corrosion are studied systematically as a function of polarization time via cyclic voltammetry and SEM. The pits are steadily increasing with polarization time, as does the voltammetric charge. In contrast, the pit density is increasing after an "induction period", then reaching a plateau and decreasing afterwards. The decrease can be explained by merging pits, therefore reducing the number of isolated pits. The lateral relative size distribution of the pits is surprisingly narrow and practically constant for all polarization times, indicating a complex growth behavior with at least three processes on very different time scales involved: After the slow induction period, where the passivating IrO_2(110) layer is locally eroded, fast undercorrosion of the unstable RuO_2(110)/Ru(0001) sets in. The dissolved Ru species in the pits are trapped, thereby decelerating the further growth of the pits. In the steady state regime the corrosion rate is determined by diffusion of dissolved Ru species through the cracks of the pits.

Supporting Information

- XP spectrum of the freshly prepared model electrode surface (Ir 4d and Ru 3d binding energy region)
- zoomed-in view of the dissolution profile
- comparison of SE micrographs before and after the SFC-ICP-MS experiment
- ToF-SIMS 3D map illustrating the layered structure of the model electrode
- ToF-SIMS 3D maps for various anion mass signals
- current density as a function of the total polarization time at 1.48 V vs. SHE
- cyclic voltammograms recorded after polarization and used for determining the voltammetric charge
- time series of histograms of the relative pit size distribution

Acknowledgements

We acknowledge financial support by the BMBF (project: 05 K2016-HEXCHEM) and by DFG (SPP2080: Ov21-16 and CH1763/3-1).

Conflict of Interest

The authors declare no conflict of interest.

Keywords: anodic corrosion · electron microscopy · mass spectrometry · oxygen evolution reaction (OER) · single-crystalline electrodes

[1] M. Carmo, D. L. Fritz, J. Mergel, D. Stolten, *Int. J. Hydrogen Energy* **2013**, *38*, 4901–4934.
[2] S. L. Scott, *ACS Catal.* **2018**, *8*, 8597–8599.
[3] T. Reier, H. N. Nong, D. Teschner, R. Schlögl, P. Strasser, *Adv. Energy Mater.* **2017**, *7*, 1601275.
[4] K. A. Stoerzinger, L. Qiao, M. D. Biegalski, Y. Shao-Horn, *J. Phys. Chem. Lett.* **2014**, *5*, 1636–1641.
[5] R. Kötz, S. Stucki, *Electrochim. Acta* **1986**, *31*, 1311–1316.
[6] N. Danilovic, R. Subbaraman, K.-C. Chang, S. H. Chang, Y. J. Kang, J. Snyder, A. P. Paulikas, D. Strmcnik, Y.-T. Kim, D. Myers, V. R. Stamenkovic, N. M. Markovic, *J. Phys. Chem. Lett.* **2014**, *5*, 2474–2478.
[7] S. Cherevko, S. Geiger, O. Kasian, N. Kulyk, J.-P. Grote, A. Savan, B. R. Shrestha, S. Merzlikin, B. Breitbach, A. Ludwig, K. J. J. Mayrhofer, *Catal. Today* **2016**, *262*, 170–180.
[8] J. Rossmeisl, A. Logadottir, J. K. Norskov, *Chem. Phys.* **2005**, *319*, 178–184.
[9] A. B. Anderson, *Electrocatalysis* **2012**, *3*, 176–182.
[10] Z. W. Seh, J. Kibsgaard, C. F. Dickens, I. Chorkendorff, J. K. Norskov, T. F. Jaramillo, *Science* **2017**, *355*, eaad4998.
[11] K. S. Exner, I. Sohrabnejad-Eskan, H. Over, *ACS Catal.* **2018**, *8*, 1864–1879.
[12] T. Binninger, R. Mohamed, K. Waltar, E. Fabbri, P. Levecque, R. Kötz, T. J. Schmid, *Sci. Rep.* **2015**, *5*, 12167.
[13] J. A. Herron, A. Morikawa, M. Mavrikakis, *PNAS* **2016**, *113*, E4937-E4945.
[14] C. Spöri, J. T. H. Kwan, A. Bonakdarpour, D. P. Wilkinson, P. Strasser, *Angew. Chem. Int. Ed.* **2017**, *56*, 5994–6021.

© 2019 The Authors. Published by Wiley-VCH Verlag GmbH & Co. KGaA

18673899, 2020, 3, Downloaded from https://chemistry-europe.onlinelibrary.wiley.com/doi/10.1002/cctc.201901674 by Justus-Liebig-Universitat, Wiley Online Library on [01/11/2022]. See the Terms and Conditions (https://onlinelibrary.wiley.com/terms-and-conditions) on Wiley Online Library for rules of use; OA articles are governed by the applicable Creative Commons License

[15] Y.-F. Li, *ChemSusChem* **2019**, *12*, 1846–1857.
[16] M. J. S. Abb, B. Herd, H. Over, *J. Phys. Chem. C* **2018**, *122*, 14725–14732.
[17] T. Weber, J. Pfrommer, M. J. S. Abb, B. Herd, O. Khalid, M. Rohnke, P. H. Lakner, J. Evertsson, S. Volkov, F. Bertram, R. Znaiguia, F. Carla, V. Vonk, E. Lundgren, A. Stierle, H. Over, *ACS Catal.* **2019**, *9*, 6530–6539.
[18] B. Herd, M. Knapp, H. Over, *J. Phys. Chem. C* **2012**, *116*, 24649–24660.
[19] I. Sohrabnejad-Eskan, A. Goryachev, K. S. Exner, L. A. Kibler, E. J. M. Hensen, J. P. Hofmann, H. Over, *ACS Catal.* **2017**, *7*, 2403–2411.
[20] S. O. Klemm, A. A. Topalov, C. A. Laska, K. J. J. Mayrhofer, *Electrochem. Commun.* **2011**, *13*, 1533–1535.
[21] S. Cherevko, *J. Electroanal. Chem.* **2017**, *787*, 11–13.
[22] S. Cherevko in *Encyclopedia of Interfacial Chemistry*, Vol. 5.1 (Ed.: K. Wandelt), Elsevier, **2018**, pp. 68–75.
[23] S. Cherevko, A. R. Zeradjanin, A. A. Topalov, N. Kulyk, I. Katsounaros, K. J. J. Mayrhofer, *ChemCatChem* **2014**, *6*, 2219–2223.
[24] P. P. T. Krause, H. Camuka, T. Leichtweiss, H. Over, *Nanoscale* **2016**, *8*, 13944–13953.
[25] T. Weber, M. J. S. Abb, O. Khalid, J. Pfrommer, F. Carla, R. Znaiguia, V. Vonk, A. Stierle, H. Over, *J. Phys. Chem. C* **2019**, *123*, 3979–3987.
[26] C. A. Schneider, W. S. Rasband, K. W. Eliceiri, *Nat. Methods* **2012**, *9*, 671–675.
[27] S. Cherevko, S. Geiger, O. Kasian, A. Mingers, K. J. J. Mayrhofer, *J. Electroanal. Chem.* **2016**, *774*, 102–110.
[28] M. Pourbaix, *Atlas of Electrochemical Equilibria in Aqueous Solutions*, Pergamon Press, **1966**.
[29] J. Juodkazytė, R. Vilkauskaitė, B. Šebeka, K. Juodkazis, *Transactions of the IMF* **2007**, *85*, 194–201.
[30] D. R. Rolison, J. W. Long, J. C. Lytle, A. E. Fischer, C. P. Rhodes, T. M. McEvoy, M. E. Bourg, A. M. Lubers, *Chem. Soc. Rev.* **2009**, *38*, 226–252.
[31] J. O'M. Bockris, A. K. N. Reddy, *Modern Electrochemistry*, Vol. 2, Plenum Publishing Corporation, New York, **1973**, pp. 991–1014.

Manuscript received: September 4, 2019
Revised manuscript received: October 15, 2019
Accepted manuscript online: October 16, 2019
Version of record online: December 5, 2019

© 2019 The Authors. Published by Wiley-VCH Verlag GmbH & Co. KGaA

18673899, 2020, 3, Downloaded from https://chemistry-europe.onlinelibrary.wiley.com/doi/10.1002/cctc.201901674 by Justus-Liebig-Universitat, Wiley Online Library on [01/11/2022]. See the Terms and Conditions (https://onlinelibrary.wiley.com/terms-and-conditions) on Wiley Online Library for rules of use; OA articles are governed by the applicable Creative Commons License